Journal of Quantitative Spectroscopy & Radiative Transfer 286 (2022) 108217

Contents lists available at ScienceDirect

Journal of Quantitative Spectroscopy & Radiative Transfer

journal homepage: www.elsevier.com/locate/jqsrt

The polarization crossfire (PCF) sensor suite focusing on satellite remote sensing of fine particulate matter $PM_{2.5}$ from space

Zhengqiang Li [a,f], Weizhen Hou [a,f,*], Jin Hong [b,**], Cheng Fan [a], Yuanyuan Wei [a], Zhenhai Liu [b], Xuefeng Lei [b], Yanli Qiao [b], Otto P. Hasekamp [c], Guangliang Fu [c], Jun Wang [d], Oleg Dubovik [e], LiLi Qie [a], Ying Zhang [a,f], Hua Xu [a,f], Yisong Xie [a], Maoxin Song [b], Peng Zou [b], Donggen Luo [b], Yi Wang [b], Bihai Tu [b]

[a] *State Environmental Protection Key Laboratory of Satellite Remote Sensing, Aerospace Information Research Institute, Chinese Academy of Sciences, Beijing 100101, P.R. China*
[b] *Anhui Institute of Optics and Fine Mechanics, Hefei Institutes of Physical Science, Chinese Academy of Sciences, Hefei 230031, P.R. China*
[c] *Netherlands Institute for Space Research (SRON, NWO-I), Utrecht NL-3584 CA, the Netherlands*
[d] *Department of Chemical and Biochemical Engineering, University of Iowa, Iowa City, IA 52242, USA*
[e] *Laboratoire d'Optique Atmosphérique (LOA), Centre National d'Etudes Spatiales (CNES), UMR 8518, University of Lille, 59000 Lille, France*
[f] *University of Chinese Academy of Sciences, Beijing 100049, P.R. China*

A R T I C L E I N F O

Article history:
Received 16 July 2021
Revised 8 April 2022
Accepted 13 April 2022
Available online 16 April 2022

Keywords:
Polarization crossfire suite
Fine particulate matter pm2.5 remote sensing
Optimal estimation inversion
Aerosol layer height
Pcf

A B S T R A C T

Focusing on satellite remote sensing of fine particulate matter $PM_{2.5}$ from space, the polarization crossfire (PCF) strategy has been developed, which includes the PCF satellite suite and the particulate matter remote sensing (PMRS) model. Expected to be the first dedicated satellite sensor for $PM_{2.5}$ remote sensing globally, the PCF suite is composed by the Particulate Observing Scanning Polarimeter (POSP) and the Directional Polarimetric Camera (DPC) together, and will be launched on board the Chinese GaoFen-5(02) satellite in 2021. Since the cross-track polarimetric measurements of POSP fully cover the multi-viewing swath of DPC, the sophisticated joint measurements could be obtained from the PCF suite in the range of 380–2250 nm including intensity and polarization, by the means of pixel matching and the cross calibration from POSP to DPC. Based on the optimal estimation inversion framework and synthetic data of PCF, the retrieval performances of key aerosol parameters are systematically investigated and assessed for the $PM_{2.5}$ estimation by the PMRS model. For the design of inversion strategy for PCF, we firstly test the retrievals of aerosol optical depth (AOD), fine mode fraction (FMF), aerosol layer height (H) and the fine-mode real part of complex refractive index (m_r^f) simultaneously with surface parameters from the synthetic PCF data, and then the columnar volume-to-extinction ratio of fine particulates (VE_f), the aerosol effective density (ρ_f) and the hygroscopic growth factor of fine-mode particles ($f(RH)$) are further obtained by the corresponding empirical relationship. The propagation errors from aerosol parameters to $PM_{2.5}$ retrieval are investigated with the key procedures of PMRS model. In addition, the influences of improving calibration accuracy of PCF on $PM_{2.5}$ retrievals are discussed, as well as the retrieval feasibility of PM_{10} by PCF strategy.

1. Introduction

As an important component of the global atmosphere, aerosols are composed of solid and liquid particles suspend in the air, which usually originate from both natural and anthropogenic sources [1,2]. Particulates with an aerodynamic diameter of less than 2.5 μm can enter the alveoli, and are usually called fine particulate matter (PM) or $PM_{2.5}$ [3], which can cause human respiratory diseases, result in serious immune system diseases, neurological diseases and cardiovascular diseases, etc., and further promote the occurrence of lung cancer [4,5]. The impact of fine PM is not only prominent in the field of environment [6] and human heath [7], it also affects the earth-atmosphere radiation balance [8–11]. In addition, atmospheric PM affect the visibility near the ground, and thus endanger the safety of public transportation, such as highways, airports, etc. [12]

* Corresponding authors: Weizhen Hou, AIRCAS, No. 9 Dengzhuang South Road, Haidian District, Beijing 100094, P.R. China.
** Corresponding author: Jin Hong, AIOFM, No. 350 Shushanhu Road, Luyang District, Hefei 230031, P.R. China
E-mail addresses: houwz@radi.ac.cn (W. Hou), hongjin@aiofm.ac.cn (J. Hong).

https://doi.org/10.1016/j.jqsrt.2022.108217

Then, how to directly and efficiently monitor large-scale atmospheric PM concentration is an important scientific and technological problem that needs to be solved urgently. The rapid development of satellite remote sensing technology provides a feasible solution for the macro-monitoring of regional atmospheric PM concentration [13]. In fact, the remote sensing capability of PM estimates largely depends on the aerosol key parameters detected by satellites [14–18]. At present, the satellite products of aerosol optical depth (AOD) are relatively mature [1,19,20–27], but the inversion accuracy of fine particles by satellite still needs to be improved. Therefore, the improvement of the detection capability of satellite sensors plays an important role in the remote sensing estimation of PM mass concentration. The multi-angle and multispectral polarimetric measurements from ultraviolet (UV) to shortwave infrared (SWIR) contain a large amount of hidden information of atmospheric PM expect for AOD, especially other important optical and microphysical characteristics [28–30]. Thus, polarization is expected to show the detailed characteristics of aerosols by the combination of multispectral or multiangle measurements, which provides strong support for retrieving the mass concentration of atmospheric PM near the ground by satellite remote sensing [31,32].

In order to simultaneously and directly monitor the PM by the satellite sensing, the polarization crossfire (PCF) strategy has been developed, which includes the PCF satellite suite and the particulate matter remote sensing (PMRS) model. The polarization crossfire (PCF) satellite suite is based on sophisticated joint measurements (including the geometric registration, band configuration and cross calibration), by the Directional Polarimetric Camera (DPC) and the Particulate Observing Scanning Polarimeter (POSP) on board the Chinese GaoFen-5 (02) satellite and Chinese Atmospheric Environmental Monitoring Satellite (DQ-1), which will be launched in the year of 2021 and 2022, respectively. Inheriting from the instrument design of Polarization and Directionality of the Earth's Reflectances (POLDER) series sensors, the first DPC instrument has been launched onboard the GaoFen-5 satellite in May 9 of 2018 in a sun-synchronous obit with the spatial resolution about 3.3 km, and 2 years of global measurements were obtained [33,34]. The POSP sensor is designed to provide polarimetric cross-track measurements by the large scanning field-of-view (FOV) from $-50°$ to $50°$ in the spectral range of 380–2250 nm with the $0.52°$ instantaneous FOV (IFOV) and about 6.4 km $\times$ 6.4 km nadir spatial resolution, which can fully cover the swath of DPC. By this means, these two PCF instruments combined allow for multiangle measurements of polarized radiance with a larger swath.

In this paper, we present the concept design of PCF satellite suite and the performance assessments of PMRS model that focus on remote sensing of $PM_{2.5}$ from space by PCF. For completeness, we briefly describe the instruments of PCF in Section 2, and then present the $PM_{2.5}$ observation method in Section 3. Afterward, the performance assessments are investigated in Section 4. We provide the discussion in Section 5 sequentially and summarize the conclusions in Section 6 finally.

2. Instruments of PCF

2.1. Instrument configuration

The PCF suite is a precise combination and matching of DPC [33] and POSP instruments, which are carried on the same satellite platform and can cover the almost coincident observation regions with the same swath width about 1850 km. Table 1 lists the specifications of PCF suite, while Fig. 1 shows the schematic diagram of PCF. In addition, Fig. 2 illustrates instrument assembly drawing of the PCF suite, which is precisely composed by the DPC and the POSP sensors.

The DPC is a POLDER-type polarization remote sensor, which uses a large FOV optical system and a wheel to switch the spectral and polarimetric channels to obtain the polarized radiation information of the atmosphere and the surface in a time-sharing manner. The DPC contains 15 detection channels, as shown in Table 1, covering a total of 8 spectral bands from 443 to 910 nm, of which 490, 670, 865 nm are polarization bands, and each polarization band uses 3 polarimetric channels (0°, 60°, 120°), the other spectral bands are all non-polarized bands, and a dark reference channel is also included for dark current correction. The new DPCs to be onboard the GaoFen-5 (02) and DQ-1 satellites are the successors model of the previous DPC onboard the GaoFen-5 (01) satellite that was launched on May 12, 2018. Although the successor has remained unchanged in terms of working mode, spectral channel, and instrument FOV, etc., some adaptive changes have been made based on the consideration of polarization crossfire, including: 1) The number of pixels of the original image sensor is increased from 512 $\times$ 512 to 1k $\times$ 1k to achieve a better field of view match between DPC and POSP; 2) The number of multiple angles has been significantly increased, and $9-17$ multiple angles can be obtained in most cases; 3) The DPC motor drive clock and sampling timing has been optimized based on the demand for simultaneous observation of the two PCF instruments.

2.1.1. POSP instrument principle

The POSP is a spaceborne multi-spectral, split-aperture, split-amplitude optical remote sensor for simultaneous polarimetric detection, its measurement principle is similar to the Aerosol Polarimetry Sensor (APS) in the failed launch of Glory Mission [35,36]. By following the scene linear polarization state, the POSP employs a pair of telescopes to measure the first three elements of Stokes vector (I, Q and U), while the fourth element V characterizing the circular polarization component of atmospheric scattering is typically at least two orders of magnitude smaller than that characterizing the linear polarization one and is considered to be essentially useless for the retrieval of atmospheric aerosols [37]. Taking the POSP optical system with a pair of optical paths as an example, which includes the scanning mirrors and telescopes (integrated by telescope lens, field stops and collimator lens), Wollaston prisms, dichroic beam splitters, focusing lens, interference filters, dual-element detectors, etc.

One of the pair of telescopes mentioned above is used to measure I and Q parameters of Stokes vector, while the other measures I and U elements. The polarization azimuth between the two telescopes in the pair is strictly limited to 45° in this optical system of POSP. Therefore, the elements of Stokes vector can theoretically be obtained from the four measured intensities:

$$\begin{bmatrix} I \\ Q \\ U \\ V \end{bmatrix} = \begin{bmatrix} I_0 + I_{90} \\ I_0 - I_{90} \\ I_{45} - I_{135} \\ 0 \end{bmatrix} \tag{1}$$

where I_0, I_{90}, I_{45} and I_{135} mean the flux elements of the four channels, respectively, and are all measured with the linear polarizer elements. Correspondingly, the degree of linear polarization (DoLP) and azimuth angle of linear polarization (AoLP) can be expressed as

$$DoLP = \frac{\sqrt{Q^2 + U^2}}{I}, \quad AoLP = \frac{1}{2} arctan\left(\frac{U}{Q}\right) \tag{2}$$

According to the requirements of PCF, the POSP instrument has been configured with 9 spectral wavelength bands, and constructed with 3 pairs of 6 independent telescopes for simultaneous polarimetric detection. The POSP measures wavelength bands of 380, 443 and 670 nm with the first telescope pair, 410, 490 and

Table 1
Specifications of the PCF suite.

No.	POSP			DPC			Main application
	Central wavelength (nm)	Spectral bandwidth(nm)	Polarization I/Q/U	Central wave-length(nm)	Spectral bandwidth (nm)	Polarization I/Q/U	
1	380	20	YES	–	–	–	Aerosol layer height, absorbing aerosol
2	410	20	YES	–	–	–	Absorbing aerosol
3	443	20	YES	443	20	NO	Aerosol, sea color
4	490	20	YES	490	20	YES	Aerosol, surface albedo, clouds
5	–	–	–	565	20	NO	Surface albedo
6	670	20	YES	670	20	YES	Aerosol properties
7	–	–	–	763	10	NO	Cloud, aerosol layer
8	–	–	–	765	40	NO	height
9	865	40	YES	865	40	YES	Land aerosol, cloud, surface
10	–	–	–	910	20	NO	Water vapor
11	1380	40	YES	–	–	–	Cirrus
12	1610	60	YES	–	–	–	Dust Aerosol
13	2250	80	YES	–	–	–	Dust aerosol, surface-atmosphere decoupling

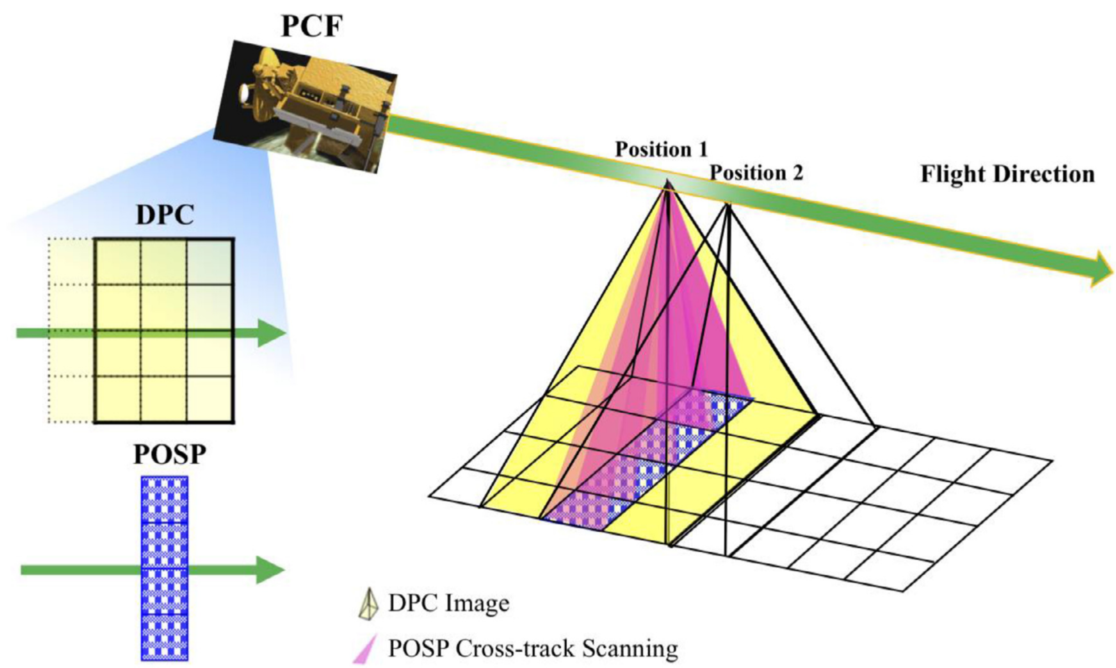

Fig. 1. The schematic diagram of PCF.

865 nm with the second pair, and 1380, 1610 and 2250 nm by the third pair.

To maintain the on-orbit detection accuracy throughout the mission, four on-board calibrators are arranged in the scan plane around the POSP scanning mirrors, including the polarized reference assembly (PRA), the unpolarized reference assembly (URA), the dark reference assembly (DRA), as well as the solar reference assembly (SRA) [38]. Among them, the calibrators PRA and URA are used for on-board polarimetric calibration, the DRA is used to establish a zero-radiation reference, while the SRA is used for on-board absolute radiometric calibration with a rationing radiometer (RR) added for tracking its possible degradation.

2.1.2. Polarization crossfire implementation strategy

Both the DPC and POSP are driven by motors when observing the earth, in which the motor of the DPC is used for sequential switching of 15 channels, while the other is used for the POSP cross-track scanning. To facilitate the joint inversion and cross calibration of the DPC and POSP on the same platform, spectral wavelength band and the FOV matching are basically needed [39]. Correspondingly, the effect of spectral matching errors can be minimized by the consistency processing of the filters of the two instruments that the filter coatings are treated in the same way in the design and processing technology to ensure the consistency of their spectral bandwidth and central wavelength, and by the measurement of the relative spectral response functions. As for the FOV matching, the main sources of the spatial mismatch between the two instruments include the stability and speed drift of the motors, as well as the systematic deviation of geolocation. Among them, the former may lead to the disorder of the spatial matching relationship between the two instruments, and at the same time cause the data processing algorithm to be complicated; while for the latter, due to the drag effect of the POSP on the FOV for the integration process and its coarser resolution, it is difficult to achieve

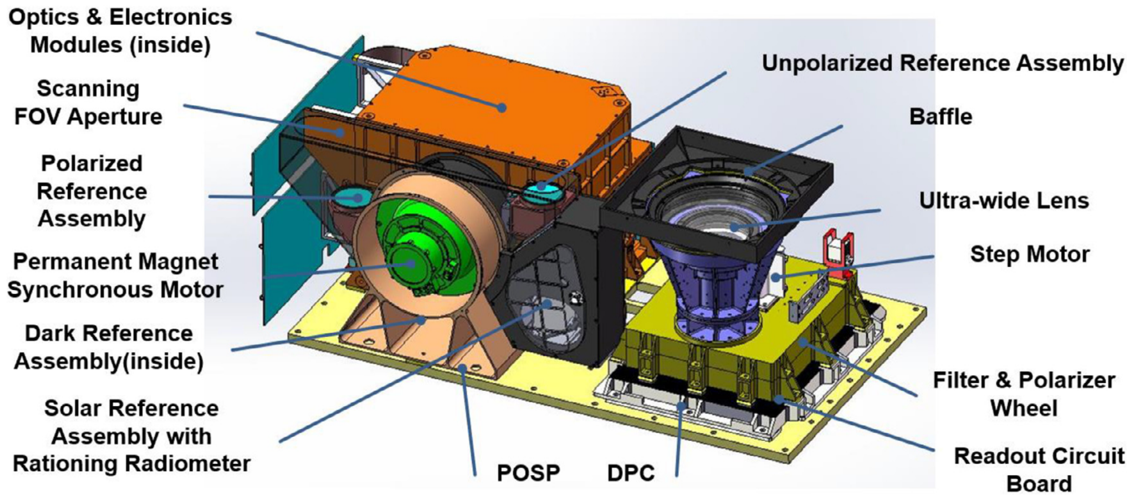

Fig. 2. Instrument assembly drawing of the PCF suite onboard DQ-1 satellite.

higher accurate geometric correction, which inevitably has a systematic deviation from the DPC.

To this end, a series of design and optimization processes have been carried out in engineering and data processing. Firstly, we use the POSP motor speed signal as the clock source of the DPC motor driver unit after being processed by the phase-locked loop (PLL), so that the DPC motor speed changes synchronously as the POSP motor speed drifts in order to avoid the accumulation of asynchronous errors between the two motors. At the same time, we set the DPC rotation speed reasonably to obtain synchronous acquisition of the specific channels of the DPC every time the POSP scans at nadir. Secondly, we use the higher original image resolution of the DPC (the original pixel number of the CCD detector is 1k $\times$ 1k, and the resolution is 1.7 km at nadir) for geometric precision correction, and the actual spatial response function of the POSP is used to achieve its FOV matching with the DPC to obtain the POSP geometric correction parameters for systematic deviations. Thus, the FOV matching processing between the POSP and DPC can be realized. Thirdly, the sinusoidal projection and multi-angle matching of the DPC images are processed after the pixel merging is completed, and the POSP geometrically corrected data is projected to the same grid as the DPC. By this means, the data sets of PCF are finally generated.

Therefore, compared with the isolated measurements of DPC, the joint polarimetric measurements of PCF are extended to UV and near-UV centered in 380 nm and 410 nm, in order to retrieve the aerosol layer height. Meanwhile, the polarimetric measurements are extended to SWIR centered in 1610 nm and 2250 nm, which can be used for surface-atmosphere decoupling and dust aerosol retrieval. Furthermore, the on-board cross calibration from POSP to DPC can be carried out, which will be discussed detailedly in Section 2.2.

2.2. On-board cross calibration

Since the POSP has a complete on-board radiometric and polarimetric calibration system, it can achieve relatively high on-board calibration accuracy, with the expected on-board radiometric calibration accuracy (ΔI) and polarimetric calibration accuracy (ΔDoLP) corresponding to within 3% and 0.005, respectively; while the DPC does not have on-board calibration capabilities with the expected accuracy of $\Delta I \leq 5\%$ and $\Delta\text{DoLP} \leq 0.02$ before cross-calibration. Therefore, the POSP can be used as a reference sensor, and the cross-calibration of the two sensors can be achieved by establishing a transfer relationship between the common wavelength bands of the POSP and DPC. Correspondingly, the theoretically expected radiometric and polarimetric accuracy of DPC can reach $\Delta I \leq 4\%$ and $\Delta\text{DoLP} \leq 0.01$ after cross-calibration, respectively.

As shown in Table 1, there are four common wavelength bands in the band configuration of PCF suite, including three polarization bands. With these two sensors of PCF assembled on the same satellite platform, the scene and observation geometric consistency errors caused by time-matching related errors can be minimized as much as possible. Meanwhile, for the common bands of the two instruments, the effect of spectral matching errors can be further minimized by the combined processing of the central wavelength and bandwidth of the filters in both instruments and accurate measurement of the relative spectral response. In comparison, FOV matching between the PCF suite is the core issue of the on-board cross calibration in data preprocessing, especially for geometrically sensitive polarization measurements. The POSP sensor works in a cross-track scanning mode, and resetting integrators used as low-pass filters in its signal conditioning circuits will inevitably cause a drag effect in its FOV. In order to solve this problem, a FOV matching approach has been proposed by considering the real spatial response function, in which the effectiveness was verified with in-flight experiments for the POSP [40].

In addition to data preprocessing, the cross-calibration modeling of the two remote sensors is another core task. Milinevsky et al. proposed a ScanPol-to-MSIP (Scanning Polarimeter to Multi-spectral Imaging Polarimeter) cross-calibration model for the FOV matching area of the two sensors in Aerosol-UA Ukrainian mission [41–43]. Besides, Zhu et al. proposed an AirPOSP-to-SIPC (Air Particulate Observing Scanning Polarimeter to Simultaneous imaging Polarization Camera) cross-calibration method and verified it by in-flight experiments in China [39], which is similar to the cross-calibration of PCF suite. While for the non-overlapping area of the FOV, the geometric difference between the scene and the sensor at the time of observation by the two remote sensors will adversely affect the polarization cross calibration results. Therefore, the cross-calibration approach to spread the FOV of POSP to the full FOV of DPC needs to be further studied, which will not be discussed in this paper.

3. PM2.5 observation method

3.1. PMRS model

Based on the vertical distribution of atmospheric particles, hygroscopicity and mass extinction efficiency, a relatively universal

Table 2
The key aerosol parameters obtained from the observation strategy of PCF for PMRS model.

Parameters	Meaning	Measurement principle	Retrieval strategy
AOD	Aerosol optical depth	Multispectral, multiangle, intensity and	[33,
FMF	Fine-mode fraction	polarization of PCF	49]
H	Equivalent parameter of aerosol layer height	380(P), 410(P) nm of PCF	[50–52]
VE_f(FMF)	columnar volume-to-extinction ratio of fine particulates	Based on the relationship of FMF	[17, 18]
$\rho_f(m_r^f)$	Effective density of fine-mode particles	Based on the real part of complex refractive index (m_r^f)	[15]
$f(RH)$	Hygroscopic growth factor	Based on the real part of complex refractive index (m_r^f)	Eq. (6)

parameterization scheme can be established to realize the conversion from the total column AOD to PM mass concentration near the ground, with the assumption that the distribution functions are ideal for vertical direction and hygroscopic growth factor [16,44–47]. The introduction of multiple parameterization schemes can effectively solve the significant nonlinear relationship between aerosol extinction and mass concentration, and even the nonlinear relationship between aerosol extinction and volume concentration [18]. This method was built based on the physical mechanism, which does not rely on ground PM concentration observations and in still applicable to those areas without ground observation stations by satellite remote sensing. By the multiple-parameterization scheme, particles with specific diameter size are separated from total suspended particles, and the near-ground optical contribution is separated from aerosol optical depth. However, the multiple parameterization scheme also means that multiple parameters are required to participate in calculation, and the PMRS model results will also be affected by the uncertainties of input key parameters. Therefore, inversion products with high-precision from the satellite plays a vital role in improving the PM retrieval accuracy from PMRS model.

The following remote sensing formula was obtained from a semi-empirical physics model for remote sensing ground-level mass concentration of fine particulate matter, named by $PM_{2.5}$ remote sensing model as follows [17,18]:

$$PM_{2.5} = AOD\frac{FMF \cdot VE_f \cdot \rho_f}{H \cdot f(RH)} \tag{3}$$

in which, there are 5 key parameters to retrieve the $PM_{2.5}$ mass concentration near the ground, AOD represents the aerosol optical depth, FMF represents the fine mode fraction, H is the equivalent parameter of aerosol layer height, VE_f is the fine-mode columnar volume-to-extinction ratio, ρ_f means the aerosol effective density of fine-mode particles, $f(RH)$ means the hygroscopic growth factor related to the chemical component and the relative humidity. Correspondingly, above factors can be considered as the own parameters of aerosols, which also can theoretically be obtained simultaneously by a multi-parameter inversion strategy [26,48] and will be discussed detailly in Section 3.2. In addition, Table 2 lists the key aerosol parameters can be obtained from the observation strategy of PCF for PMRS model.

In particular, the VE_f is usually dependent on the FMF and can be represented by the form of quadratic polynomial of FMF [18], while ρ_f also has a relationship with the real part of complex refractive index of fine particulate (m_r^f). Thus, as long as these 4 key aerosol parameters, including AOD, FMF, H and m_r^f, are firstly retrieved by PCF satellite remote sensing, and then other 3 key aerosol parameters VE_f, ρ_f and $f(RH)$ can be further calculated easily. Fig. 3 illustrates the evaluation scheme of the $PM_{2.5}$ retrieval potential from PCF measurements, in which, the item of multiplying AOD and FMF is usually noted as fine-mode AOD (AOD_f) and can be directly retrieved from polarimetric sensors [33].

The aerosol vertical model driven by the equivalent parameter of aerosol layer height (H) was used to simplify the aerosol vertical distribution in the real atmosphere. The aerosol relative distribution with altitude is assumed as a Gaussian function [51,53–58], and can be written in the form of

$$h(z) = A\exp\left(-4\ln 2(z-H_c)^2/\sigma^2\right), \tag{4}$$

where H_c is the aerosol layer height and corresponds to the center height of the Gaussian function, σ means the width of the aerosol height distribution with a typical value in the range of 100 m to 2000 m in this study, but the value of σ is fixed in retrieval due to insufficient information content for inversion test, and A represents a normalization factor. The Gaussian function of aerosol layer distribution can usually peak at the surface or below, and we just consider the part above the surface for the inversion test in this study [50,51]. In addition, $H = g(H_c,\sigma)$, here g is the function of H_c and σ, which means the ratio of AOD and the extinction efficient near surface.

As mentioned above, another key parameter VE_f is usually dependent on FMF. Thus, the fine-mode AOD can be converted to volume concentration with multiplying by VE_f. Zhang and Li (2015) firstly confirmed the relationship of FMF-VE_f can be expressed as follows [18]:

$$VE_f = 0.2887FMF^2 - 0.4663FMF + 0.356\ (0.1 \le FMF \le 1.0) \tag{5}$$

We assumed the real part of complex refractive index of dry fine particles $m_{r,dry}^f$ and water $m_{r,water}^f$ as constant value of 1.53 and 1.33, respectively [59–61]. Then, the hygroscopic growth factor can be calculated from the m_r^f of wet and dry fine particles as follow

$$f(RH) = 1/\left(1 - \frac{m_r^f - m_{r,dry}^f}{m_{r,water}^f - m_{r,dry}^f}\right) \tag{6}$$

Consequently, the volume concentration can be converted to mass concentration by multiplying density. The research in Wei et al. (2021) showed the practicability of deriving density from the real part of complex refractive index (m_r^f) based on satellite [15]. The following empirical function was used in this study to calculate the density of fine mode aerosol.

$$\frac{\left(m_r^f\right)^2 - 1}{\left(m_r^f\right)^2 + 2} = c \cdot \rho_f^d, \tag{7}$$

where m_r^f represents the fine-mode m_r, c and d were fitted parameters with $c = 0.19$ and $d = 0.9$.

3.2. Inversion strategy

Following the optimal-estimation (OE) based inversion framework, the cost function $J(\mathbf{x})$ can be represented as

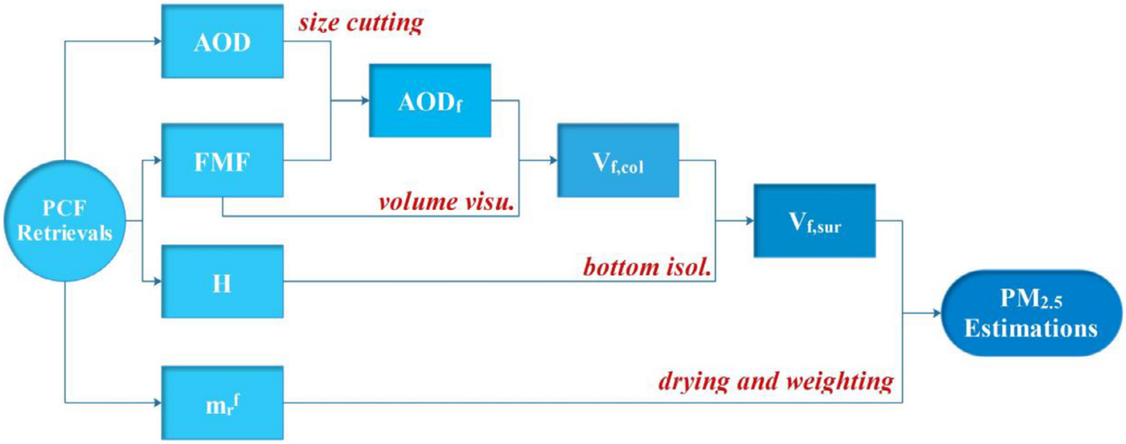

Fig. 3. Evaluate scheme of the $PM_{2.5}$ retrieval potential from PCF.

$$J(\mathbf{x}) = \tfrac{1}{2}[\mathbf{y} - \mathbf{F}(\mathbf{x}, \mathbf{b})]^T\ \mathbf{S}_\epsilon^{-1}\ [\mathbf{y} - \mathbf{F}(\mathbf{x}, \mathbf{b})] + \tfrac{1}{2}(\mathbf{x} - \mathbf{x}_a)^T\ \mathbf{S}_a^{-1}\ (\mathbf{x} - \mathbf{x}_a) \tag{8}$$

where y means an observation vector of PCF, **F** means a forward model, **x** means a state vector of the retrieval, **b** means the corresponding vector of aerosol model, in which **x** contains the variables of state being retrieved and **b** contains the variables of state that are assumed. In addition, $\mathbf{S}_\varepsilon$ represents the observation error covariance matrix and is determined by the measurement error and model error together, $\mathbf{x}_a$ is the a priori estimate of state vector, and $\mathbf{S}_a$ corresponds to the error covariance matrix of a priori state vector. For the retrieval of those parameters contained in state vector, we minimize the objective function $J(\mathbf{x})$ optimally subject to (s.t.) the lower bound **l** and upper bounds **u** by optimized iterations [1,33,62], that is

$$\begin{aligned} &\min\ J(\mathbf{x}) \\ &\text{s.t.}\,\mathbf{l} \le \mathbf{x} \le \mathbf{u} \end{aligned} \tag{9}$$

For the multi-angular, multispectral, intensity and polarimetric measurements of DPC in PCF suite, the measurements at 5 wavelength bands are used, including 443, 490(P), 565, 670(P), and 865(P) nm, which can be denoted as $\lambda_3, \lambda_4, \lambda_5, \lambda_6$ and λ_9 in sequence. In addition, the denoted bands λ_4, λ_6 and λ_9 are for polarization detection, while λ_3 and λ_5 represent the only intensity measurements. Consequently, the observational vector **y** of DPC can be defined as in the form of

$$\mathbf{y}_{DPC} = [\mathbf{y}^{\nu_1},\ \mathbf{y}^{\nu_2}, \cdots,\ \mathbf{y}^{\nu_m}]^T \tag{10}$$

and

$$\mathbf{y}^{\nu_j} = \left[I_{\lambda_3}^{\nu_j}, \cdots, I_{\lambda_6}^{\nu_j},\ I_{\lambda_9}^{\nu_j}, DoLP_{\lambda_3}^{\nu_j}, \cdots, DoLP_{\lambda_6}^{\nu_j},\ DoLP_{\lambda_9}^{\nu_j}\right]^T,\ \ (j = 1, \cdots, m) \tag{11}$$

where the superscript v_m means the sequence of multi-viewing angle, and m means the number of used multiangle measurements. Here, I means the intensity component and the definition of $DoLP$ is the same as Eq. (2).

While for the single-viewing, multispectral and polarimetric measurements of POSP integrated in PCF suite, 8 wavelength bands centered in 380(P), 410(P), 443(P), 490(P), 670(P), 865(P), 1610(P) and 2250(P) nm are employed, and the observational vector **y** of POSP can be represented as

$$\begin{aligned} \mathbf{y}_{POSP} = [&I_{\lambda_1}, \cdots, I_{\lambda_4}, I_{\lambda_6}, I_{\lambda_9}, I_{\lambda_{12}}, I_{\lambda_{13}}, DoLP_{\lambda_1}, \\ &\cdots, DoLP_{\lambda_4}, DoLP_{\lambda_6}, DoLP_{\lambda_9}, DoLP_{\lambda_{12}}, DoLP_{\lambda_{13}}]^T \end{aligned} \tag{12}$$

As for the simulation of PCF, which can be combined by the measurements of DPC and POSP as:

$$\mathbf{y}_{PCF} = [\mathbf{y}_{DPC}, \mathbf{y}_{POSP}\ ]^T \tag{13}$$

For the surface reflectance model setting in inversion, an improved bidirectional reflectance distribution function (BRDF) model is used in order to decrease the number of retrieved multispectral BRDF parameters [33,63,64], which can be represented in the form as

$$r_\lambda(\theta_0, \theta_v, \varphi) = f(\lambda)[1 + k_1 f_{\text{geom}}(\theta_0, \theta_v, \varphi) + k_2 f_{\text{vol}}(\theta_0, \theta_v, \varphi)] \tag{14}$$

where $f(\lambda)$ represents the wavelength-dependent model parameter, k_1 and k_2 are the wavelength-independent linear model parameters, which correspond to the coefficients of geometric-optical kernel (f_{geom}) and volumetric kernel (f_{vol}). The values of both kernels only depend on the observation geometry (θ_0,θ_v,φ), in which, θ_0 and θ_v are the solar zenith angles and viewing zenith angle respectively, φ is the relative azimuth angle calculated by the solar azimuth angles (φ_0) and viewing azimuth angle (φ_v). Meanwhile, a bidirectional polarized reflectance distribution function (BPDF) model developed by Maignan et al. (2009) was also integrated in the surface reflectance matrix, which mainly depends on a free linear model parameter C, the normalized difference vegetation index (NDVI) and the observation geometry [65,66].

For the inversion from PCF measurements, we define the state vector as

$$\begin{aligned} \mathbf{x}_{PCF} = [&AOD(\lambda_0), FMF(\lambda_0), H, m_r^f(\lambda_0), f(\lambda_1), \\ &\cdots, f(\lambda_6), f(\lambda_9), f(\lambda_{12}), f(\lambda_{13}), k_1, k_2, C]^T \end{aligned} \tag{15}$$

where AOD, FMF and m_r^f are all selected at the reference wavelength $\lambda_0 = 550$ nm, which will be detailedly discussed in Section 4.1, H means the aerosol layer height, $f(\lambda)$ is the wavelength-dependent surface parameter of improved BRDF model, k_1 and k_2 are the wavelength independent linear model parameters [33,63], and C is the only free linear parameter of BPDF model and depends on the surface type [65]. Correspondingly, the state vector for PCF totally include 4 aerosol parameters, 11 BRDF parameters and 1 BPDF parameter.

Based on the degree of freedom for signal (DFS) results for information content analysis in the previous work [28,33,34,67,68], the information content of aerosol parameters (including AOD, FMF, m_r^f) and surface parameters (including $f(\lambda)$, k_1, k_2, C) are all sufficient. However, for the parameters of aerosol vertical distribution in Eq. (4), only the DFS of center height H_c can meet the

Table 3
Effective radius and variance of each mode for forward simulation and inversion.

	Fine-mode aerosols			Coarse-mode aerosols	
	Mode 1	Mode 2	Mode 3	Mode 4	Mode 5
$r_{\mathrm{eff}\,(\mu m)}$	0.094	0.163	0.282	0.882	1.759
$v_{\mathrm{eff}\,(\mu m)}$	0.130	0.130	0.130	0.284	1.718

retrieval demanding, while the width σ still is difficult to be retrieved due to insufficient information content [53,69,70]. Therefore, we exclude the parameter σ from the retrieval state vector, and then assume a fixed value of σ equal to 2000 m for inversion test in this study. Besides, the spatially-distributed width of the vertical profile of aerosol concentration can be further globally obtained based on statistical methods from the climatology measurements of Cloud-Aerosol Lidar with Orthogonal Polarization (CALIOP) [55,58,71].

4. Performance assessment

4.1. Assessment framework

To investigate theoretical capability of PCF measurements for the retrieval of aerosol key parameters, the inversion tests are carried out based on the synthetic measurements simulated by following the PCF satellite observation mode. The spectral response functions of DPC and POSP instruments are respectively applied, a perfect spatial match of two instruments are assumed, and the corresponding theoretical random noises affected by the instrument calibrations and signal-to-noise ratio (SNR) are also considered. The SRON (Netherlands Institute for Space Research) forward model and inversion codes with a multimode setup are used in this study [72–75]. Here, the multimode setting in SRON represents the aerosol model is a multimodal distribution instead of a bimodal distribution, and each mode has fixed size distribution parameters with a fixed effective radius and effective various [76].

The particle size distribution for each mode is assumed to be lognormal:

$$\frac{dN(r)}{d\ln(r)} = \frac{N_0}{\sqrt{2\pi}\ln\sigma_g}\exp\left[-\frac{1}{2}\left(\frac{\ln r-\ln r_g}{\ln\sigma_g}\right)^2\right] \tag{16}$$

where N_0 is the total number concentration of particles of each mode, r_g and σ_g are the geometric number mean radius and standard deviation of each mode, respectively. We can further convert the geometric parameters r_g and σ_g to the effective radius r_{eff} and the effective variance v_{eff} by the equation as [77,78]

$$\begin{cases} r_{\mathrm{eff}} = r_g\, exp\left(\frac{5}{2}\ln^2\sigma_g\right) \\ v_{\mathrm{eff}} = exp\left(\ln^2\sigma_g\right) - 1 \end{cases} \tag{17}$$

In this study, the multimode retrieval based on five modes are used with fine modes (Mode 1–3) and coarse modes (Mode 4–5), the corresponding effective radius and effective variance are listed in Table 3 [79]. For the fine-mode aerosols, we assumed they are all spherical and composed by the inorganic matter with black carbon; while for the coarse modes, we assumed they are non-spherical and composed by the dust with inorganic matter. Therefore, the fraction of spherical particles (f^c_{sph}) of coarse-mode aerosols also needs to be included in the retrieval state vector [26,75].

While for the complex refractive index of fine-mode (Mode 1–3) and coarse-mode (Mode 4–5) aerosols, they can be written uniformly by the form of

$$m^{\mathrm{f,\ c}} = m_{\mathrm{r}}^{\mathrm{f,c}} + i\cdot m_{\mathrm{i}}^{\mathrm{f,\ c}} \tag{18}$$

where m_{r} and m_{i} represent the real and imaginary part, the superscript f and c represent the fine mode and coarse mode, respectively. Besides, we assume that the fine-mode aerosols have the same spectral complex refractive index for Mode 1–3, and the coarse-mode aerosols have another same spectral complex refractive index for Mode 4–5. Therefore, we do not need to retrieve the wavelength-dependent parameters $m^{\mathrm{f}}(\lambda)$ and $m^{\mathrm{c}}(\lambda)$ directly, but try to construct them by the equation of

$$m^{\mathrm{f,c}}(\lambda) = \sum_{k=1}^{2}\alpha_k^{\mathrm{f,c}}\; m_k^{\mathrm{f,c}}(\lambda) \tag{19}$$

where m_k^{f} and m_k^{c} ($k = 1,\ 2$) are the standard spectral refractive index from the work of the D'Almeida et al. [80], thus we only have to retrieve the mode component coefficients $\alpha_k^{\mathrm{f,c}}$ in the inversion by SRON. Here, by following the assumptions of fine-mode and coarse-mode aerosols setting in SRON, $m_1^{\mathrm{f}}(\lambda)$ and $m_2^{\mathrm{f}}(\lambda)$ represent the standard spectral complex refractive index of the inorganic matter and the black carbon, respectively; while $m_1^{\mathrm{c}}(\lambda)$ and $m_2^{\mathrm{c}}(\lambda)$ corresponds to the standard spectral complex refractive index for the dust and the inorganic matter, respectively.

Correspondingly, the retrieval state vector in Eq. (15) can be equivalent to the form of

$$\begin{aligned} x = [\ & N_0^1, N_0^2, N_0^3, N_0^4, N_0^5,\ \ \alpha_1^{\mathrm{f}}, \alpha_2^{\mathrm{f}}, \alpha_1^{\mathrm{c}}, \alpha_2^{\mathrm{c}}, f_{sph}^c, H, f(\lambda_1), \\ & \cdots, f(\lambda_6), f(\lambda_9), f(\lambda_{12}), f(\lambda_{13}), k_1, k_2, C]^T \end{aligned} \tag{20}$$

where $N_0^1, N_0^2, N_0^3, N_0^4$ and N_0^5 mean the total number of particles of five modes, α_1^{f} and α_2^{f} are the fine-mode component coefficients to construct the complex refractive index, α_1^{c} and α_2^{c} are the corresponding coarse-mode component coefficients, f_{sph}^c is the spherical fraction of coarse-mode aerosols, and the definitions of BRDF and BPDF parameters are same as Eq. (15). The detailed elements of state vector by SRON are further listed in Table 4. Subsequently, the aerosol model vector **b** can be represented as

$$\begin{aligned} b = [&\sigma,\ r_{\mathrm{eff}}^1, r_{\mathrm{eff}}^2, r_{\mathrm{eff}}^3, r_{\mathrm{eff}}^4, r_{\mathrm{eff}}^5, v_{\mathrm{eff}}^1, v_{\mathrm{eff}}^2, v_{\mathrm{eff}}^3, v_{\mathrm{eff}}^4, v_{\mathrm{eff}}^5, m_1^{\mathrm{f}}(\lambda), \\ & m_2^{\mathrm{f}}(\lambda), m_1^{\mathrm{c}}(\lambda),\ \ m_2^{\mathrm{c}}(\lambda)]^T \end{aligned} \tag{21}$$

where σ is the layer width of Gaussian function for aerosol height distribution, $r_{\mathrm{eff}}^1, r_{\mathrm{eff}}^2, r_{\mathrm{eff}}^3, r_{\mathrm{eff}}^4$ and r_{eff}^5 are the effective radius of five modes listed in Table 3, $v_{\mathrm{eff}}^1, v_{\mathrm{eff}}^2, v_{\mathrm{eff}}^3, v_{\mathrm{eff}}^4$ and v_{eff}^5 correspond to the effective variance, $m_1^{\mathrm{f}}(\lambda), m_2^{\mathrm{f}}(\lambda), m_1^{\mathrm{c}}(\lambda)$ and $m_2^{\mathrm{c}}(\lambda)$ are the standard spectral refractive index defined in Eq. (18).

Based on the retrieval state vector **x** and predefined aerosol model **b** the spectral aerosol optical depth $\tau_{\mathrm{a}}^i(\lambda)$ of each mode can be further calculated by [78]

$$\tau_{\mathrm{a}}^i(\lambda) = N_0^i\; C_{ext}^i(\lambda), (i = 1, 2, \cdots, 5) \tag{22}$$

where C_{ext} is the extinction cross-section, and equals to the product result of geometric cross-section and extinction efficiency factor. Consequently, the spectral AOD, fine-mode AOD and FMF can be obtained by

$$\begin{cases} AOD(\lambda) = \sum\limits_{i=1}^{5}\tau_{\mathrm{a}}^i(\lambda) \\ AOD_{\mathrm{f}}(\lambda) = \sum\limits_{i=1}^{3}\tau_{\mathrm{a}}^i(\lambda) \\ FMF(\lambda) = \frac{AOD_{\mathrm{f}}(\lambda)}{AOD(\lambda)} \end{cases} \tag{23}$$

The synthetic measurements of PCF are also simulated by SRON based on five assumed aerosol modes [76] by considering the theoretical measurement errors of PCF, which are mainly affected the instrument SNR and calibrations errors (ΔI and $\Delta DoLP$). Table 5 shows the combined parameters of assumed true aerosol and surface properties, which are generated stochastically in the reasonable ranges. In order to determine the relative total number concentration between all 5 modes, the random results of fine-mode

Table 4
The elements in state vector for the inversion test by SRON.

	Parameter name	Elements in X
Aerosol properties	Aerosol loading	$N_0^i,\ (i = 1,\ 2, \cdots, 5)$
	Coarse-mode spherical fraction	f_{sph}^c
	Refractive index coefficients	$\alpha_k^f,\ \alpha_k^c,\ (k = 1, 2)$
	Aerosol layer height	H
Surface properties	Scaling parameter for BPDF model	C
	Coefficient of Li sparse kernel	k_1
	Coefficient of Ross thick kernel	k_2
	BRDF scaling parameters	$f(\lambda_i),(i = 1, \cdots, 6, 9, 12, 13)$
	Number of aerosol parameters	11
	Number of surface parameters	12
	Length of the state vector	23

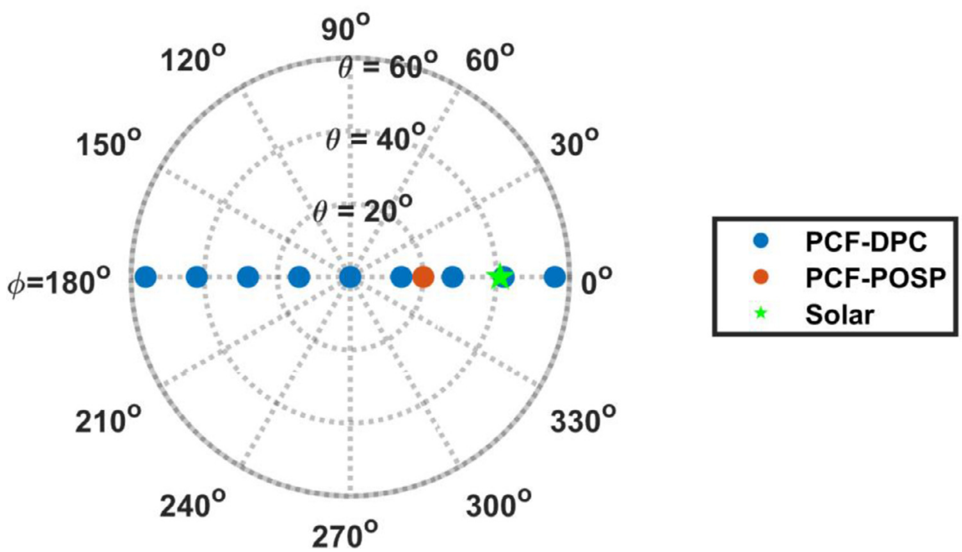

Fig. 4. The corresponding polar plot for the PCF-DPC and PCF-POSP geometry.

Table 5
Parameters to create for the synthetic measurements (based on 500 random samples).

Parameters	Range
Fine-mode AOD	$0.005 \sim 0.7$ at 550nm
Coarse-mode AOD	$0.005 \sim 0.3$ at 550nm
Spherical index	$0 \sim 1.0$
Aerosol layer height (m)	$1000 \sim 6000$
Width of height (m)	$100 \sim 2000$
Components of fine mode	Mix of inorganic matter and black carbon
Components of coarse mode	Mix of dust and inorganic matter
Surface parameter	Mix of soil and grass

AOD (Mode 1–3) in the range of $0.005 \sim 0.7$ and coarse-mode AOD (Mode 4–5) in the range of $0.005 \sim 0.3$ are used. Among them, the relative concentrations of Mode 1–3 are randomly distributed to constrain the value of fine-mode AOD, while the random relative concentrations of Mode 4–5 are also randomly adjusted to determine the value of coarse-mode AOD. Correspondingly, the first 3 elements of Stokes vector were simulated at a satellite representative height of about 800 km. Here, we assumed the radiance error $\Delta I = 4\%$ and a polarization error $\Delta DoLP = 0.01$ for DPC sensor after cross calibration of PCP, as well as $\Delta I = 3\%$ and $\Delta DoLP = 0.005$ for POSP sensor, with the form of a relative error (ΔI) and an absolute error ($\Delta DoLP$), respectively [33,34,81]. By considering the calibration error as the measurement error, the synthetic measurement vector of PCF ($\mathbf{y}_{PCF}$) has been systematically obtained with the random noise added.

Based on a set of typical observation geometries are shown in the Fig. 4, there are 500 synthetic samples used for performing the investigations of PCF. For the reason that the range of scattering angle (Θ) for expected PCF observation is mainly between 80° and 180° in most cases, we set the theoretical observation geometries in the principal plane with a solar zenith angle $\theta_0 = 41°$ for simplicity, which can cover the similar wide-range scattering angle from 83° to 179°. The synthetic measurements of each sample contain at least 9 viewing angles spaced between ±56° from nadir in the principal plane for the PCF-DPC and one randomly-given viewing zenith angle ($\theta_v = 20°$) between the large scanning FOV of ±50° for the PCF-POSP.

4.2. Aerosol parameters retrieval

In order to evaluate the inversion accuracy of key aerosol parameters, the statistical parameters including the root mean square error (RMSE) and mean absolute error (MAE) are employed together, as well as the correlation coefficient (R^2). Fig. 5 shows the key aerosol parameters that related to the $PM_{2.5}$ retrieval from the PCF measurements. Fig. 5(a) and (b) illustrate the AOD and FMF retrieval results versus the truth results all at 550 nm for inversion test, respectively. For the inversion test by SRON, the first three of the five aerosol modes can be considered as the fine modes, and other two are the coarse modes [76]. For the calculation of FMF, the extinction coefficients of the fine particle modes are added up and divided by total extinction. The retrieval uncertainties are very small for both error evaluation parameters, in which the RMSE is 0.024 for AOD and 0.08 for FMF, while the MAE corresponds

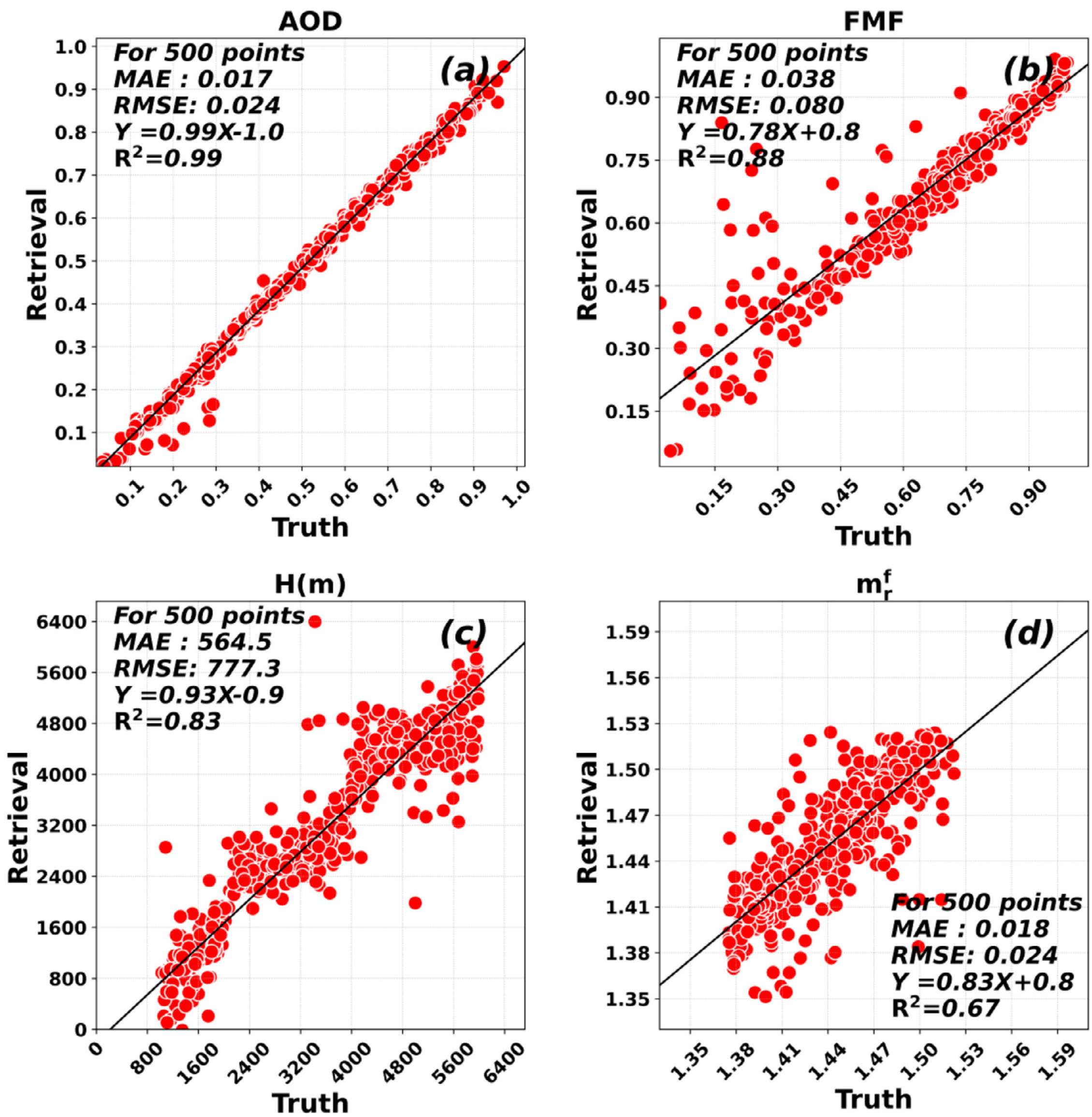

Fig. 5. Scatterplot of the retrievals of AOD (a), FMF (b), H (c), and m_r^f (d) versus the truth results for synthetic scenes, in which the 3 key parameters AOD, FMF and m_r^f are normalized at 550 nm.

to 0.017 and 0.038, respectively. Meanwhile, the correlation coefficients (R^2) are 0.99 for the AOD and 0.88 for the FMF. In our inversion test, the AOD retrieval results have a good consistency with the reference AOD in most value ranges, but scatterplot of the FMF results are relatively discrete in the low value area. However, the FMF $\geq$ 0.8 case is usually dominated by the anthropogenic aerosols, which also corresponds to the main application scenario of PCF satellites. For the case of low FMF, natural sand and dust are still the majority, which is not the main case considered in this study.

The values of aerosol layer heights (H) are assumed varying randomly in the range of 1000 m to 6000 m with the width σ varying randomly from 100 m to 2000 m by following the Gaussian distribution in the forward simulations, while the value of σ is fixed to 2000 m in the inversion test because of the insufficient information content. Besides, we assume that only one aerosol layer is presented in the atmosphere. Fig. 5(c) shows the scatterplot of retrieved H results versus the truth aerosol layer heights, in which RMSE is 777.3 m, MAE is 564.5 m and R^2 is 0.83, respectively. Here, the retrievals of aerosol layer heights are mainly depending on intensity and polarization measurements of PCF-POSP in the UV and near-UV wavelength channels in this assessment [52]. Besides, the 763 and 765 nm O_2 A-band channels of DPC could potentially provide significant additional constraint on aerosol height [53,70], which will make higher precision aerosol layer height retrieval possible and provide favorable support for $PM_{2.5}$ retrieval by PMRS model in our further study [51]. Moreover, Fig. 5(d) show the scatterplot of retrieved m_r^f versus truth results at wavelength 550 nm, in which, the RMSE is 0.024, MAE is 0.018, and R^2 is 0.67. In natural environment, the value of m_r is generally greater than or equal to 1.33 (e.g. the pure water) at 550 nm. Among these particles that are composed of the same dry composition, the larger the value of m_r is, the drier of the aerosols usually will be. However, particles with a high dry m_r (e.g., ammonium sulfate) can take up water and still have an effective m_r that is significantly greater than dry particles with a naturally lower m_r (e.g. sea salt).

4.3. PM2.5 mass concentration

Based on PMSE model, the $PM_{2.5}$ retrieval results (shown in Fig. 6) can be obtained from PCF synthetic data by PMRS model. The assumed truth values on the X-axis represent $PM_{2.5}$ results

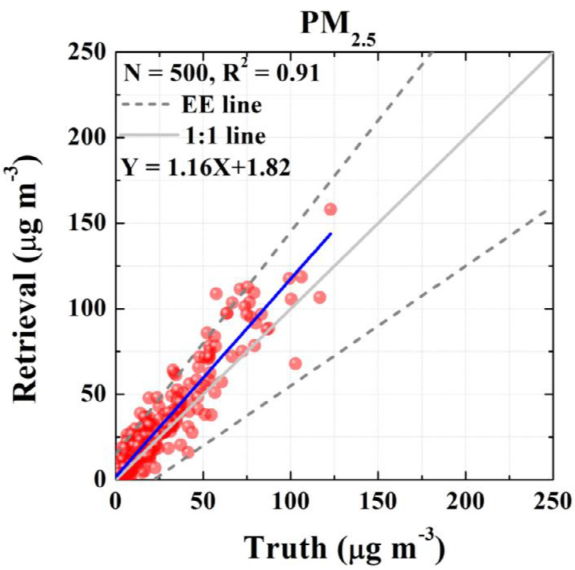

Fig. 6. The scatterplot of the assumed truth and the retrieved $PM_{2.5}$ results with an expected error (EE) of $\pm(30\%PM_{2.5}+15)\ \mu g\ m^{-3}$.

calculated by assumed key aerosol parameters without error, while the retrieval values on the Y-axis represent $PM_{2.5}$ results retrieved from PCF synthetic data by considering the accumulation of errors in inversion. Correspondingly, the MAE is 5.21 $\mu g\ m^{-3}$ and the RMSE is 7.88 $\mu g\ m^{-3}$ for scatterplot of 500 sample points, respectively. Meanwhile, the slope (1.16) and bias (1.82 $\mu g\ m^{-3}$) of the fitting line implies that most scattering plots are close to 1:1 line. The research of Zhang et al. (2020) has pointed out that the PMRS model has an expected error (EE) of $\pm(30\%PM_{2.5}+15)\ \mu g\ m^{-3}$ [82]. In this study, the proportion of the samples involved within the EE lines is about 96.6%, and there is a good correlation (with R^2 of 0.91) between the assumed truth and retrieved $PM_{2.5}$ values. It should be note that several results with large relative errors are extreme cases in synthetic data (for example, extreme case with $PM_{2.5}<1\ \mu g\ m^{-3}$ and AOD_f is about 0.25), which is unlikely appearing in the real atmosphere.

In general, the $PM_{2.5}$ retrieval results by PMRS model mainly depend on the retrieval uncertainties of corresponding key aerosol parameters. The above tests have assumed that the inversion knowns key aspects of the simulated system of PMRS are relative perfect, and thus the results may inevitably overestimate $PM_{2.5}$ to certain extent. In a comprehensive view, the inherent assumptions of PMRS model additional to the retrieval uncertainties of the inputs, can contribute to the estimation error of $PM_{2.5}$ in Fig. 6. These main assumptions include: (1) the volume-to-extinction ratio is fitted as a function of FMF; (2) the mass density is approximate to a function of the real refractive index based on the electromagnetic polarization; (3) the real refractive index is also used to approximately determine the hygroscopic growth factor; (4) the simulated Gaussian model is served as the aerosol profile; (5) the dependence of the particle properties (such as aerosol particle size) on vertical profile is neglected. Subsequently, the influence of PMRS model on PCF's ability to retrieve $PM_{2.5}$ will be further discussed in the next section.

5. Discussion

5.1. PMRS model procedure influence on PCF's PM2.5

The PMRS model itself inevitably has certain uncertainties. Fig. 7 (a-e) actually represent the impact of above five procedures on $PM_{2.5}$ estimations and these corresponding errors. The X-axis represents the assumed truth (input) values, and the Y-axis represents the corresponding retrieval results. The result of multiplying AOD and FMF is used to calculate the extinction contribution of $PM_{2.5}$, a good correlation (with R^2 of 0.99) and a slight deviation was found in Fig. 7(a) suggesting the good consistency between the input and output values of AOD × FMF. Hence, small uncertainties were caused by the size cutting procedure.

As for volume visualization procedure in Eq. (5), the AOD is converted to volume concentration through VE_f(FMF) model. The relatively large uncertainty of FMF, especially for small FMF retrievals, can be transferred directly to VE_f values, which caused some plots were far away from 1:1 line in Fig. 7(b). The mass density weighting procedure in Fig. 7(d) was realized by using the semi-empirical relationship between ρ_f and m_r^f in Eq. (7). Since the small fluctuation ranges of VE_f and ρ_f, the uncertainties caused by the volume visualizing procedure, and weighting procedure, are both relatively small. The bottom isolation procedure is conducted by using PCF retrievals of aerosol layer height through Eq. (4). Then, the ratio of extinction coefficient near the ground to the total aerosol optical depth can be obtained. The fitting line of the scattering plots in Fig. 7(c) has a slope close to 1 and a small offset. Compared with the other procedures, there is a higher cost performance of effectively improving the accuracy of aerosol layer height retrieval.

As for the hygroscopic growth factor drying procedure in Fig. 7(e) was realized by Eq. (6). Here, the real part of the refractive index is used to approximately estimate the $f(RH)$ from satellite. The uncertainties of $f(RH)$ may come from the retrieval errors of the input m_r^f, or the assumed value of the dry particulate matter. The aerosol hygroscopic properties of aerosol particles are related to their chemical composition. Under the same environmental humidity, the hygroscopic growth factors of different aerosol types are obviously different ranging from 1.0 to 3.0 [83]. If the chemical composition of particles is the same, with the increase of ambient humidity, the value of hygroscopic growth factor will also increase [84]. Direct humidity correction from satellite data depends on the development of sensors and the improvement of inversion techniques in the future.

5.2. Error propagation on PM2.5 by PCF

Along with the semi-empirical physics model for $PM_{2.5}$ estimate by Eq. (3), the modeling errors originating from retrieval set up with the parameters in Table 5 inevitably constitute a significant $PM_{2.5}$ error sources, which mainly include: (1) the width of Gaussian distribution profile is fixed in the retrieval but simulated with a variety across two magnitudes (from 0.1 - 2 km); (2) the fine and coarse aerosol modes are relatively fixed in their size distribution; (3) two aerosol types are modified from a particular combination of dust/inorganic aerosols and black carbon/inorganic aerosols; (4) limited surface type that mixes soil and grass.

In order to investigate the propagated errors of the PMRS model by PCF for the $PM_{2.5}$, we assume the independent errors for PMRS model and input parameters in this study. Based on the error propagation theory, total errors on $PM_{2.5}$ can be written as

$$\frac{\Delta PM_{2.5}}{PM_{2.5}}=\sqrt{\left(\frac{\Delta AOD}{AOD}\right)^2+\left(\frac{\Delta FMF}{FMF}\right)^2+\left(\frac{\Delta H}{H}\right)^2+\left(\frac{\Delta m_r^f}{m_r^f}\right)^2+(\Delta PMRS_{model})^2} \tag{24}$$

where $\frac{\Delta AOD}{AOD}$, $\frac{\Delta FMF}{FMF}$, $\frac{\Delta H}{H}$ and $\frac{\Delta m_r^f}{m_r^f}$ represent the mean relative error of four key aerosol parameters retrieved by SRON, respectively, in which ΔH already contains the propagated errors from H_c and σ with assumed Gaussian function of aerosol layer distribution. Besides, $\Delta PMRS_{model}$ means the model error of PMRS, which cover

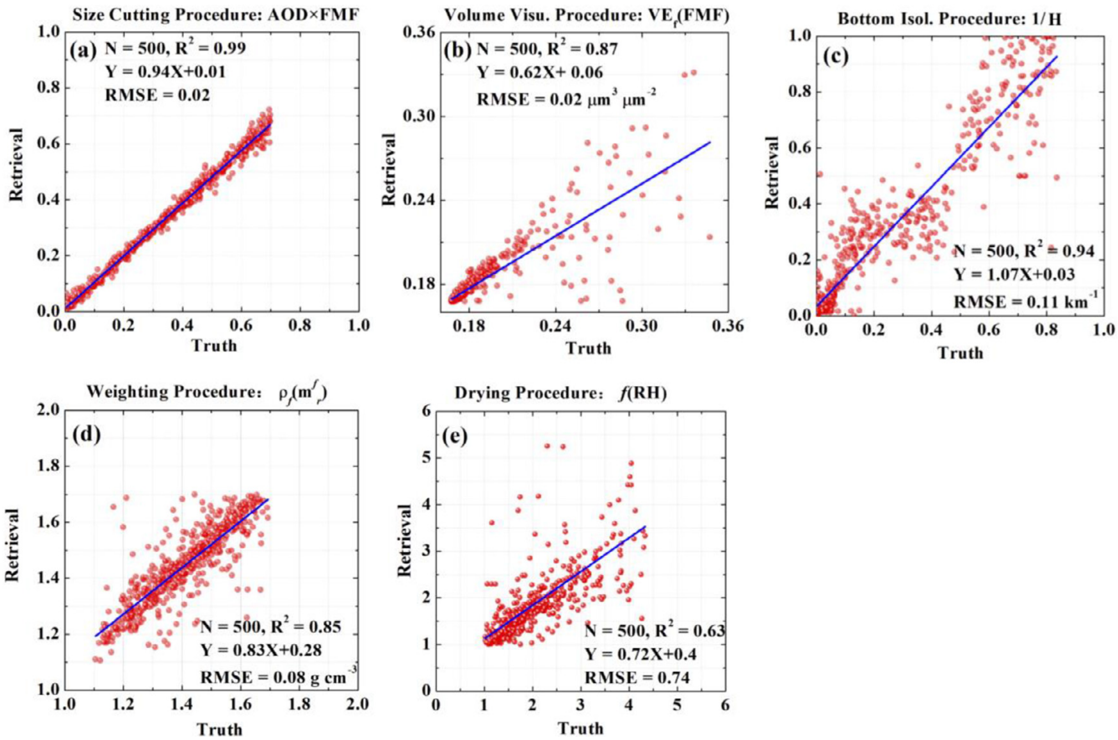

Fig. 7. The errors propagation of PMRS model procedures including (a) size cutting procedure, (b) volume visualization procedure, (c) bottom isolation procedure, (d) mass density weighting procedure, and (e) hygroscopic growth factor drying procedure.

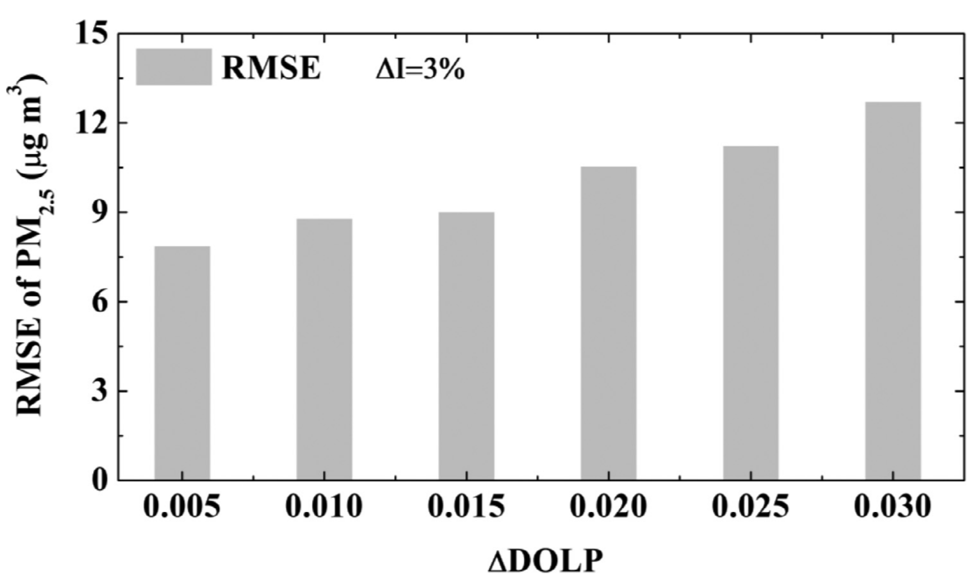

Fig. 8. The RMSE of $PM_{2.5}$ under the different calibration accuracy of ΔDoLP.

the total uncertainty of PMRS model regardless the uncertainties of measurement parameters for $PM_{2.5}$ retrieval [18].

Correspondingly, Table 6 lists the input parameter errors for PMRS model and result of error propagation, in which, the individual errors of 4 key aerosol parameters (AOD, FMF, H and m_r^f) are based the retrieval results in Fig. 5, and the retrieval error of AOD has been adjusted by the actual inversion results of SRON [76]. Moreover, the relative error of PMRS model is set to an empirical value with 34%, which has been detailedly discussed in the work of Zhang & Li (2015) [18], and uncertainties from other sources

Table 6
The individual errors of 4 key aerosol parameters for PMRS model and result of error propagation.

Error source	Individual errors	
4	AOD	11.75%
key	FMF	14.88%
aerosol	H	20.56%
parameters	m_r^f	8.15%
PMRS model error	34.00%	
Total error	44.77%	

have almost all been considered. By this means, the propagated error can be calculated from the PMRS model error and the input parameter errors (retrieval errors of AOD, FMF, H and m_r^f), and the total error of $PM_{2.5}$ by PCF is about 44.77% in this study, which can be regarded as the an upper bound for the retrieval error of $PM_{2.5}$ with the actual PCF measurements in most case. Besides, Li et al. (2016) have used in-situ measurements to estimate $PM_{2.5}$ based on PMRS model, in which the total error of $PM_{2.5}$ was around the value of 31% [17]. Therefore, the error envelope of $\pm(30\%PM_{2.5} + 15)$ $\mu g/m^3$ in Fig. 6 is reasonable for inversion test in this study.

5.3. PM2.5 accuracy dependence on the crossfire calibration of PCF

To analyze the importance of the radiance and polarization accuracy for the aerosol parameters related to PMRS model, we performed aerosol retrievals based on different calibration accuracies. By fixing the value of $\Delta I = 3\%$ and $\Delta DoLP = 0.005$ for PCF-POSP, we conduct a test with an assuming ideal radiance accuracy ($\Delta I = 3\%$) and the changing $\Delta DoLP$ from 0.005 to 0.03 with the interval 0.005 for PCF-DPC, which is different from the actual measurement uncertainty estimates of DPC described in Section 2.2. Based on the aerosol parameters retrieved from the PCF synthetic data, we further analyze the $PM_{2.5}$ mass concentration retrieved by the PMRS model in Fig. 8. Based on our preliminary simulation results, as the $\Delta DoLP$ improves from 0.03 to 0.005, the retrieval accuracy of $PM_{2.5}$ is gradually improving. However, this improvement become less obvious when the accuracy is increased to a certain extent even the calibration of the PCF can reach to 0.005. We will conduct further research to demonstrate the specific impact of the on-orbit calibration on the polarimetric satellite sensors on $PM_{2.5}$ estimation.

6. Conclusions

As an innovative polarimetric satellite remote sensing sensor, the polarization crossfire (PCF) suite is based on the sophisticated joint observations by the particulate observing scanning polarimeter (POSP) and directional polarimetric camera (DPC) on board GaoFen-5 (02) and DQ-1 satellites to be launched in 2021 and 2022, and focus on satellite remote sensing of $PM_{2.5}$ from space. Since the cross-track polarimetric measurements of POSP fully cover the multi-viewing swath of DPC, the multispectral, multiangle, intensity and polarized measurements could be obtained from the PCF suite in the range of 380–2250 nm, by the means of pixel matching and the cross calibration from POSP to DPC. Based on the optimal estimation inversion framework and synthetic data of PCF, the retrieval performances of key aerosol parameters are systematically investigated and assessed for the $PM_{2.5}$ estimation by the particulate matter remote sensing (PMRS) model, which further demonstrate the feasibility and rationality of the PCF strategy. In this paper, our work can be summarized as follows.

(1) Based on the PMRS semi-empirical model, there are five key parameters used to retrieve the $PM_{2.5}$ mass concentration near the ground. Among these key parameters, the columnar volume-to-extinction ratio VE_f is represented as an empirical function of FMF, while the aerosol effective density ρ_f and hygroscopic growth factor $f(RH)$ also can be written as functions of m_r^f. Therefore, for the design of inversion strategy for PCF, we firstly choose to test the retrievals of AOD, FMF, H and m_r^f together from the synthetic PCF data, and then the performance assessments of PMRS model are quantitatively discussed and evaluated in this paper.

(2) With the expected radiance calibration error and polarization calibration error setting of PCF, and by considering the representative observation geometries and various parameters setting, the synthetic data are simulated and these four key aerosol parameters (AOD, FMF, H and m_r^f) are simultaneously retrieved with corresponding surface parameters. Three statistical parameters including the root mean square error (RMSE), mean absolute error (MAE) and correlation coefficient (R^2) are used to evaluate the retrieval results versus the assumed truth results. For the AOD retrieval, the expected result of RMSE, MAE and R^2 corresponds to 0.03, 0.02 and 0.99, respectively; while for the FMF retrieval, the result of RMSE, MAE and R^2 is about 0.08, 0.04 and 0.90. Besides, the RMSE, MAE and R^2 is about 780 m, 570 m and 0.83 for the retrieval of aerosol layer height (H). In addition, the RMSE, MAE and R^2 is about 0.03, 0.02 and 0.67 for the retrieval of m_r^f, in which the correlation coefficient is relative lower than those results of other 3 aerosol parameters.

(3) The errors propagation to $PM_{2.5}$ estimation are also investigated with corresponding procedures including the size cutting, volume visualization, bottom isolation, hygroscopic growth factor drying procedure and weighting procedure sequentially, in which the bottom isolation procedure has a significantly greater weight than other procedures. Therefore, we can find that improving the retrieval accuracy of aerosol layer height is much more important. This study provides an important guiding significance for further improving the sensor and detection mechanism. In addition, the influences of improving calibration accuracy on $PM_{2.5}$ estimations are discussed, and the RMSE of derived $PM_{2.5}$ decreases monotonically as the improvement of polarization calibration accuracy.

The PCF suite can observe the global distribution of $PM_{2.5}$ mass concentrations. In addition, the PCF can also provide coarse-mode m_r (m_r^c) and then the effective density of coarse mode particles could be determined. Meanwhile, the fine-mode VE_f, coarse-mode VE_c and suspended particles could be retrieved together by PCF strategy, in which the strategy to obtain VE_c for coarse mode can refer to the work of Wei et al. (2020) [85]. Therefore, the possibility of PM_{10} (particulates with an aerodynamic diameter of less than 10 μm) estimation can be explored based on PCF satellite measurements and PMRS model in the future.

Declaration of Competing Interest

The authors declare that we have no financial and personal relationships with other people or organizations that can inappropriately influence our work, there is no professional or other personal interest of any nature or kind in any product, service and/or company that could be construed as influencing the position presented in, or the review of, the manuscript entitled “The polarization crossfire (PCF) sensor suite focusing on satellite remote sensing of fine particulate matters PM2.5 from space”.

CRediT authorship contribution statement

Zhengqiang Li: Conceptualization, Methodology, Funding acquisition. **Weizhen Hou:** Methodology, Funding acquisition. **Jin Hong:** Conceptualization, Methodology, Funding acquisition. **Cheng Fan:** Methodology. **Yuanyuan Wei:** Methodology. **Zhenhai Liu:** Methodology. **Xuefeng Lei:** Conceptualization. **Yanli Qiao:** Conceptualization. **Otto P. Hasekamp:** Methodology. **Guangliang Fu:** Methodology. **Jun Wang:** Methodology. **Oleg Dubovik:** Methodology. **LiLi Qie:** Methodology. **Ying Zhang:** Methodology. **Hua Xu:** Funding acquisition. **Yisong Xie:** Methodology. **Maoxin Song:** Conceptualization. **Peng Zou:** Conceptualization. **Donggen Luo:** Conceptualization. **Yi Wang:** Conceptualization. **Bihai Tu:** Conceptualization.

Acknowledgements

This work was supported by the National Outstanding Youth Foundation of China (Grant No. 41925019), the National Natural Science Foundation of China (Grant No. 41871269), the K. C. Wong Education Foundation (Grant No. GJTD-2018–15), and the National Natural Science Foundation of China (Grant Nos. 42101365, 41671364). J. Wang's contribution to this work is made possible via the in-kind support (James E. Ashton Professorship) in the University of Iowa.

Reference

[1] Hou W, Wang J, Xu X, Reid JS, Janz SJ, Leitch JW. An algorithm for hyperspectral remote sensing of aerosols: 3. application to the GEO-TASO data in KORUS-AQ field campaign. J Quant Spectrosc Radiat Transfer 2020;253: 107161.
[2] Zubko V, Kaufman YJ, Burg RI, Martins JV. Principal component analysis of remote sensing of aerosols over oceans. IEEE Trans Geosci Remote Sens 2007;45:730 -45.
[3] Lin C-I, Tsai C-H, Sun Y-L, Hsieh W-Y, Lin Y-C, Chen C-Y, et al. Instillation of particulate matter 2.5 induced acute lung injury and attenuated the injury recovery in ACE2 knockout mice. Int J Biol Sci 2018;14:253 -65.
[4] Brook RD, Rajagopalan S, Pope III CA, JR Brook, A Bhatnagar, AV Diez-Roux, et al. Particulate matter air pollution and cardiovascular disease: an update to the scientific statement from the. Am Heart Assoc Circul 2010;121:2331 -78.
[5] Kampa M, Castanas E. Human health effects of air pollution. Environ Pollut 2008;151:362 -7.
[6] Zhang Y., Shao K., Tang X., Li J. The study of urban photochemical smog pollution in China. Acta Scicentiarum Naturalum Universitis Pekinesis. 1998.
[7] Song C, He J, Wu L, Jin T, Chen X, Li R, et al. Health burden attributable to ambient PM2.5 in China. Environ Pollut 2017;223:575 -86.
[8] Li X, Wagner F, Wei P, Yang J, Mauzerall DL. Reduction of solar photovoltaic resources due to air pollution in China. Proc Natl Acad Sci 2017;114:201711462.
[9] Ångström A. Atmospheric turbidity, global illumination and planetary albedo of the earth. Tellus 1964;14:435 -50.
[10] Sokolik IN. Radiation balance and solar radiation spectrum. In: Jørgensen SE, Fath BD, editors. Encyclopedia of ecology. Oxford: Academic Press; 2008. p. 2951. -5.
[11] Grau E, Gastellu-Etchegorry J-P. Radiative transfer modeling in the earth–atmosphere system with DART model. Remote Sens Environ 2013;139:149 -70.
[12] Wang KC, Dickinson RE, Su L, Trenberth KE. Contrasting trends of mass and optical properties of aerosols over the Northern Hemisphere from 1992 to 2011. Atmos Chem Phys 2012;12:9387 -98.
[13] Yang L, Xu H, Jin Z. Estimating spatial variability of ground-level PM2.5 based on a satellite-derived aerosol optical depth product: fuzhou, China. Atmos Pollut Res 2018;9:1194 -203.
[14] Wei Y, Li Z, Zhang Y, Chen C, Dubovik O, Zhang Y, et al. Validation of POLDER GRASP aerosol optical retrieval over China using SONET observations. J Quant Spectrosc Radiat Transfer 2020;246:106931.
[15] Wei Y, Li Z, Zhang Y, Chen C, Xie Y, Lv Y, et al. Derivation of PM10 mass concentration from advanced satellite retrieval products based on a semi-empirical physical approach. Remote Sens Environ 2021;256:112319.
[16] Yan X, Shi W, Li Z, Li Z, Luo N, Zhao W, et al. Satellite-based PM2. 5 estimation using fine-mode aerosol optical thickness over China. Atmos Environ 2017;170:290–302.
[17] Li Z, Zhang Y, Shao J, Li B, Hong J, Liu D, et al. Remote sensing of atmospheric particulate mass of dry PM2.5 near the ground: method validation using ground-based measurements. Remote Sens Environ 2016;173:59–68.
[18] Zhang Y, Li Z. Remote sensing of atmospheric fine particulate matter (PM2.5) mass concentration near the ground from satellite observation. Remote Sens Environ 2015;160:252 -62.
[19] Chen C, Dubovik O, Fuertes D, Litvinov P, Lapyonok T, Lopatin A, et al. Validation of GRASP algorithm product from POLDER/PARASOL data and assessment of multi-angular polarimetry potential for aerosol monitoring. Earth Syst Sci Data 2020;12:3573–620.
[20] Dubovik O, Li Z, Mishchenko MI, Tanré D, Karol Y, Bojkov B, et al. Polarimetric remote sensing of atmospheric aerosols: instruments, methodologies, results, and perspectives. J Quant Spectrosc Radiat Transfer 2019;224:474–511.
[21] Choi M, Kim J, Lee J, Kim M, Park Y-J, Jeong U, et al. GOCI yonsei aerosol retrieval (YAER) algorithm and validation during the DRAGON-NE Asia 2012 campaign. Atmos Meas Tech 2016;9:1377 -98.
[22] Gupta P, Levy RC, Mattoo S, Remer LA, Munchak LA. A surface reflectance scheme for retrieving aerosol optical depth over urban surfaces in MODIS Dark Target retrieval algorithm. Atmos Meas Tech 2016;9:3293 -308.
[23] Sayer AM, Govaerts Y, Kolmonen P, Lipponen A, Luffarelli M, Mielonen T, et al. A review and framework for the evaluation of pixel-level uncertainty estimates in satellite aerosol remote sensing. Atmos Meas Tech 2020;13:373–404.
[24] Hsu NC, Jeong MJ, Bettenhausen C, Sayer AM, Hansell R, Seftor CS, et al. Enhanced deep blue aerosol retrieval algorithm: the second generation. J Geophys Res 2013;118:9296 -315.
[25] Tanré D, Bréon F, Deuzé J, Dubovik O, Ducos F, François P, et al. Remote sensing of aerosols by using polarized, directional and spectral measurements within the a-train: the PARASOL mission. Atmos Meas Tech 2011;4:1383 -95.
[26] Dubovik O, Herman M, Holdak A, Lapyonok T, Tanré D, Deuzé JL, et al. Statistically optimized inversion algorithm for enhanced retrieval of aerosol properties from spectral multi-angle polarimetric satellite observations. Atmos Meas Tech 2011;4:975–1018.
[27] Diner DJ, Martonchik JV, Kahn RA, Pinty B, Gobron N, Nelson DL, et al. Using angular and spectral shape similarity constraints to improve MISR aerosol and surface retrievals over land. Remote Sens Environ 2005;94:155 -71.
[28] Hou W, Li Z, Wang J, Xu X, Goloub P, Qie L. Improving remote sensing of aerosol microphysical properties by near-infrared polarimetric measurements over vegetated land: information content analysis. J Geophys Res 2018;123:2215 -43.
[29] Fougnie B, Marbach T, Lacan A, Lang R, Schlüssel P, Poli G, et al. The multi--viewing multi-channel multi-polarisation imager – overview of the 3MI polarimetric mission for aerosol and cloud characterization. J Quant Spectrosc Radiat Transfer 2018;219:23–32.
[30] Fougnie B, Chimot J, Vázquez-Navarro M, Marbach T, Bojkov B. Aerosol retrieval from space – how does geometry of acquisition impact our ability to characterize aerosol properties. J Quant Spectrosc Radiat Transfer 2020;256:107304.
[31] Dubovik O, Schuster GL, Xu F, Hu Y, Bösch H, Landgraf J, et al. Grand challenges in satellite remote sensing. Front Remote Sensing 2021;2:619818.
[32] Zhang Y, Li Z, Bai K, Wei Y, Xie Y, Zhang Y, et al. Satellite remote sensing of atmospheric particulate matter mass concentration: advances, challenges, and perspectives. Fundamental Res 2021;1:240 -58.
[33] Li Z, Hou W, Hong J, Zheng F, Luo D, Wang J, et al. Directional polarimetric camera (DPC): monitoring aerosol spectral optical properties over land from satellite observation. J Quant Spectrosc Radiat Transfer 2018;218:21–37.
[34] Zheng F, Hou W, Li Z. Optimal estimation retrieval for directional polarimetric camera onboard Chinese Gaofen-5 satellite: an analysis on multi-angle dependence and a posteriori error. Acta Physica Sinica 2019;68:040701.
[35] Mishchenko MI, Cairns B, Hansen JE, Travis LD, Kopp G, Schueler CF, et al. Accurate monitoring of terrestrial aerosols and total solar irradiance: introducing the Glory mission. Bull Am Meteorol Soc 2007;88:677 -91.
[36] El-Habashi A, Bowles J, Foster R, Gray D, Chami M. Polarized observations for advanced atmosphere-ocean algorithms using airborne multi-spectral hyper-angular polarimetric imager. J Quant Spectrosc Radiat Transfer 2021;262:107515.
[37] Hansen JE, Travis LD. Light scattering in planetary atmospheres. Space Sci Rev 1974;14:527–610.
[38] Persh S., Shaham Y.J., Benami O., Cairns B., Mishchenko M.I., Hein J.D., et al. Ground performance measurements of the Glory Aerosol Polarimetry sensor. Conference on earth observing systems XV. San Diego, CA2011.
[39] Zhu S, Hong J, Li Z, Lei X, Zou P, Liu Z, et al. Radiometer-to-imager in-flight cross calibration and verification. Opt Express 2020;28:11001.
[40] Lei X, Zhu S, Li Z, Hong J, Liu Z, Tao F, et al. Integration model of POSP measurement spatial response function. Opt Express 2020;28:25480.
[41] Milinevsky G, Yatskiv Y, Degtyaryov O, Syniavskyi I, Mishchenko M, Rosenbush V, et al. New satellite project Aerosol-UA: remote sensing of aerosols in the terrestrial atmosphere. Acta Astronaut 2016;123:292–300.
[42] Syniavskyi I, Oberemok Y, Ivanov Y, Sosonkin M, Quan C. Multispectral polarization state analyzer of scanning polarimeter scanpol. Int J Opt 2020;2020:1–15.
[43] Syniavskyi I, Oberemok Y, Danylevsky V, Bovchaliuk A, Fesianov I, Milinevsky G, et al. Aerosol-UA satellite mission for the polarimetric study of aerosols in the atmosphere. J Quant Spectrosc Radiat Transfer 2021;267:107601.
[44] Chen Q-X, Yuan Y, Huang X, Jiang Y-Q, Tan H-P. Estimation of surface-level PM2. 5 concentration using aerosol optical thickness through aerosol type analysis method. Atmos Environ 2017;159:26–33.
[45] Lin C, Li Y, Yuan Z, Lau AK, Li C, Fung JC. Using satellite remote sensing data to estimate the high-resolution distribution of ground-level PM2. 5. Remote Sens Environ 2015;156:117 -28.
[46] Chu DA, Tsai T-C, Chen J-P, Chang S-C, Jeng Y-J, Chiang W-L, et al. Interpreting aerosol lidar profiles to better estimate surface PM2. 5 for columnar AOD measurements. Atmos Environ 2013;79:172 -87.
[47] Tsai T-C, Jeng Y-J, Chu DA, Chen J-P, Chang S-C. Analysis of the relationship between MODIS aerosol optical depth and particulate matter from 2006 to 2008. Atmos Environ 2011;45:4777 -88.
[48] Dubovik O, Lapyonok T, Litvinov P, Herman M, Fuertes D, Ducos F, et al. GRASP: a versatile algorithm for characterizing the atmosphere. SPIE Newsroom 2014.
[49] Zhang Y, Li Z, Liu Z, Zhang J, Qie L, Xie Y, et al. Retrieval of the fine-mode aerosol optical depth over east china using a grouped residual error sorting (GRES) method from multi-angle and polarized satellite data. Remote Sens (Basel) 2018;10:1838.
[50] Wu L, Hasekamp O, van Diedenhoven B, Cairns B. Aerosol retrieval from multiangle, multispectral photopolarimetric measurements: importance of spectral range and angular resolution. Atmos Meas Tech 2015;8:2625 -38.
[51] Wu L, Hasekamp O, van Diedenhoven B, Cairns B, Yorks JE, Chowdhary J. Passive remote sensing of aerosol layer height using near-UV multiangle polarization measurements. Geophys Res Lett 2016;43:8783 -90.
[52] Qie L., Li D., Li Z., Zhang Y., Hou W., Chen X. A sensitivity study of atmospheric reflectance to aerosol layer height based on multi-angular polarimetric measurements. 2015;9678:96780V.

[53] Chen X, Xu X, Wang J, Diner DJ. Can multi-angular polarimetric measurements in the oxygen-A and B bands improve the retrieval of aerosol vertical distribution? J Quant Spectrosc Radiat Transfer 2021;270:107679.
[54] Xu X, Wang J, Wang Y, Zeng J, Torres O, Yang Y, et al. Passive remote sensing of altitude and optical depth of dust plumes using the oxygen A and B bands: first results from EPIC/DSCOVR at lagrange-1 point. Geophys Res Lett 2017;44:7544 -54.
[55] Xu X, Wang J, Wang Y, Zeng J, Torres O, Reid JS, et al. Detecting layer height of smoke aerosols over vegetated land and water surfaces via oxygen absorption bands: hourly results from EPIC/DSCOVR in deep space. Atmos Meas Tech 2019;12:3269 -88.
[56] Diner DJ, Boland SW, Brauer M, a Bruegge, Burke KA, Chipman R, et al. Advances in multiangle satellite remote sensing of speciated airborne particulate matter and association with adverse health effects: from MISR to MAIA. J Appl Remote Sens 2018;12(4):042603.
[57] Ding S, Wang J, Xu X. Polarimetric remote sensing in oxygen A and B bands: sensitivity study and information content analysis for vertical profile of aerosols. Atmos Meas Tech 2016;9:2077 -92.
[58] Zeng Z-C, Chen S, Natraj V, Le T, Xu F, Merrelli A, et al. Constraining the vertical distribution of coastal dust aerosol using OCO-2 O2 A-band measurements. Remote Sens Environ 2020;236:111494.
[59] Shingler T, Sorooshian A, Ortega A, Crosbie E, Wonaschütz A, Perring AE, et al. Ambient observations of hygroscopic growth factor and f(RH) below 1: case studies from surface and airborne measurements. J Geophys Res 2016;121(13):13661–77 -1377.
[60] Shingler T, Crosbie E, Ortega A, Shiraiwa M, Zuend A, Beyersdorf A, et al. Airborne characterization of subsaturated aerosol hygroscopicity and dry refractive index from the surface to 6.5 km during the SEAC4RS campaign. J Geophys Res 2016;121:4188 -210.
[61] Chen J, Li Z, Lv M, Wang Y, Wang W, Zhang Y, et al. Aerosol hygroscopic growth, contributing factors, and impact on haze events in a severely polluted region in northern China. Atmos Chem Phys 2019;19:1327 -42.
[62] Hou W, Wang J, Xu X, Reid JS, Han D. An algorithm for hyperspectral remote sensing of aerosols: 1. Development of theoretical framework. J Quant Spectrosc Radiat Transfer 2016;178:400 -15.
[63] Litvinov P, Hasekamp O, Cairns B. Models for surface reflection of radiance and polarized radiance: comparison with airborne multi-angle photopolarimetric measurements and implications for modeling top-of-atmosphere measurements. Remote Sens Environ 2011;115:781 -92.
[64] Xie D, Cheng T, Wu Y, Fu H, Zhong R, Yu J. Polarized reflectances of urban areas: analysis and models. Remote Sens Environ 2017;193:29–37.
[65] Maignan F, Bréon F-M, Fédèle E, Bouvier M. Polarized reflectances of natural surfaces: spaceborne measurements and analytical modeling. Remote Sens Environ 2009;113:2642 -50.
[66] Ge B, Mei X, Li Z, Hou W, Xie Y, Zhang Y, et al. An improved algorithm for retrieving high resolution fine-mode aerosol based on polarized satellite data: application and validation for POLDER-3. Remote Sens Environ 2020;247:111894.
[67] Hou W, Wang J, Xu X, Reid JS. An algorithm for hyperspectral remote sensing of aerosols: 2. Information content analysis for aerosol parameters and principal components of surface spectra. J Quant Spectrosc Radiat Transfer 2017;192:14–29.
[68] Hou W., Li Z., Zheng F., Qie L. Retrieval of aerosol microphysical properties based on the optimal estimation method: information content analysis for satellite polarimetric remote sensing measurements. International archived of the photogrammetry, remote sensing and spatial information sciences, ISPRS TC III Mid-term Symposium "Development, Technologies and Applications in Remote Sensing". Beijing. 2018. p. 533 -7.
[69] Hou WZ, Wang HF, Li ZQ, Qie LL, Ge BY, Fan C, et al. Preliminary sensitivity study of aerosol layer height from synthetic multiangle polarimetric remote sensing measurements. ISPRS - international archives of the photogrammetry. Remote Sensing Spatial Inform Sci 2019 XLII-3/W9:63-9.
[70] Chen X, Wang J, Xu X, Zhou M, Zhang H, Castro Garcia L, et al. First retrieval of absorbing aerosol height over dark target using TROPOMI oxygen B band: algorithm development and application for surface particulate matter estimates. Remote Sens Environ 2021;265:112674.
[71] Liu Z, Mortier A, Li Z, Hou W, Goloub P, Lv Y, et al. Improving daytime planetary boundary layer height determination from CALIOP: validation based on ground-based lidar station. Adv Meteorol 2017;2017:5759074.
[72] Hasekamp OP, Litvinov P, Butz A. Aerosol properties over the ocean from PARASOL multiangle photopolarimetric measurements. J Geophys Res 2011;116:D14204.
[73] Hasekamp OP, Landgraf J. Retrieval of aerosol properties over land surfaces: capabilities of multiple-viewing-angle intensity and polarization measurements. Appl Opt 2007;46:3332 -44.
[74] Schepers D, aan de Brugh JMJ, Hahne P, Butz A, Hasekamp OP, Landgraf J. LINTRAN v2.0: a linearised vector radiative transfer model for efficient simulation of satellite-born nadir-viewing reflection measurements of cloudy atmospheres. J Quant Spectrosc Radiat Transfer 2014;149:347 -59.
[75] Fu G, Hasekamp O, Rietjens J, Smit M, Di Noia A, Cairns B, et al. Aerosol retrievals from different polarimeters during the ACEPOL campaign using a common retrieval algorithm. Atmos Meas Tech 2020;13:553 -73.
[76] Fu G, Hasekamp O. Retrieval of aerosol microphysical and optical properties over land using a multimode approach. Atmos Meas Tech 2018;11:6627 -50.
[77] Wang J, Xu X, Ding S, Zeng J, Spurr R, Liu X, et al. A numerical testbed for remote sensing of aerosols, and its demonstration for evaluating retrieval synergy from a geostationary satellite constellation of GEO-CAPE and GOES-R. J Quant Spectrosc Radiat Transf 2014;146:510 -28.
[78] Xu X, UNL-VRTM Wang J. A testbed for aerosol remote sensing: model developments and applications. In: Kokhanovsky A, editor. Springer series in light scattering, springer series in light scattering. Springer; 2019. p. 1–69.
[79] Fan C, Fu G, Noia AD, Smit M, Rietjens JHH, Ferrare RA, et al. Use of a neural network-based ocean body radiative transfer model for aerosol retrievals from multi-angle polarimetric measurements. Remote Sens (Basel) 2019;11:2877.
[80] D'Almeida GA, Koepke P, Shettle EP. Atmospheric aerosols: global climatology and radiative characteristics. Hampton, VA, USA: A Deepak Pub; 1991.
[81] Dubovik O, Li Z, Mishchenko MI, Tanre D, Karol Y, Bojkov B, et al. Polarimetric remote sensing of atmospheric aerosols: instruments, methodologies, results, and perspectives. J Quant Spectrosc Radiat Transfer 2019;224:474–511.
[82] Zhang Y, Li Z, Chang W, Zhang Y, de Leeuw G, Schauer JJ. Satellite observations of PM2.5 changes and driving factors based forecasting over China 2000–2025. Remote Sens (Basel) 2020;12:2518.
[83] Liu X, Cheng Y, Zhang Y, Jung J, Sugimoto N, Chang S-Y, et al. Influences of relative humidity and particle chemical composition on aerosol scattering properties during the 2006 PRD campaign. Atmos Environ 2008;42:1525 -36.
[84] Chen J, Zhao CS, Ma N, Yan P. Aerosol hygroscopicity parameter derived from the light scattering enhancement factor measurements in the North China Plain. Atmos Chem Phys 2014;14:8105 -18.
[85] Wei Y, Li Z, Zhang Y, Chen J, Lv Y. Estimation of total suspended particles (TSP) mass concentration based on sun sky photometer and lidar. SPIE; 2020.